Kernel mode decomposition for time-frequency localization of transient flow: The formation of a laminar separation bubble

Tso-Kang Wang and Kourosh Shoele ●*

Department of Mechanical Engineering, Joint College of Engineering,
Florida State University–Florida A&M University, Tallahassee, Florida 32310, USA

Identifying and tracking transient fluid responses has long been challenging due to the inherent and correlated complexities in both spatial and temporal domains. Kernel mode decomposition (KMD) is a newly proposed method capable of capturing the transitioning amplitude and frequency locally. In this study we extend the KMD with a sparsification network that groups the response modes based on their spectral and spatial proximity using an energylike index to instigate systems with transitional behaviors. A synthetic problem setup is used to demonstrate how the proposed method can identify essential modes with changing both amplitude and frequencies. A two-sided oscillating lid-driven cavity flow problem demonstrates that the KMD network can further track the transition of modes even when spatial distributions vary over time. Finally, we inspect the formation process of a laminar separation bubble with the proposed method and isolate multiple competing mechanisms involved in the process. These results reveal that KMD can extend the application of modal analysis methods to identify transitioning spatial structures associated with varying frequency in an interpretable fashion, a necessary step for their use for understanding broad dynamic systems.

I. INTRODUCTION

Transient responses are ubiquitous observations in many dynamic systems, such as compliant blood vessels experiencing periodic pulsing motion from the heartbeat, a wind gust exerting a large dynamic pressure fluctuation on the airfoil structure, and how the atmosphere flow coherent structures format and dissipate. However, it has long been difficult to study the responses of these systems during and after the transient phenomena due to the lack of suitable analysis tools. The extension of classic modal analysis techniques to systems with transient responses has been of continuous interest to many research communities. For example, the multiresolution dynamic mode decomposition (mrDMD) [1] and multiscale proper orthogonal decomposition (mPOD) [2] were proposed to filter the data into different spectral scales and to separate dynamics with distinct temporal behaviors. In practice, however, these methods are more suitable for systems with clear scale separation. The windowed DMD (wDMD) [3] performs dynamic mode decomposition (DMD) with a sliding window to extract spatial modes with transitioning frequencies. This global method, as an extension of DMD, could not efficiently track the local spatial feature associated to the frequency change. On the other hand, another class of empirical mode decomposition (EMD) methods [4] has been adopted for analyses of systems with transitional behaviors. This includes fluid structure interaction [5], epidemiology [6], financial engineering [7], geographic studies [8],

---

*kshoele@eng.famu.fsu.edu

064401-1

and structural monitoring [9], just to name a few. The EMD, also known as the Hilbert-Huang transformation (HHT), decomposes a signal by recursively removing the intrinsic mode functions (IMFs) from the signal until a constant trend is left. The most common procedure to acquire the IMFs is through the "sifting" process, which connects the extrema of the signal and finds the mean of their interpolated curves. EMD is capable of extracting the instantaneous frequencies through the IMFs and is adaptive to various applications. Nevertheless, EMD, by its nature, is a heuristic approach, and the sifting process along with the intermediate models are difficult to interpret and correlate to physical phenomena. Recently, artificial neural networks (ANNs) have been employed for pattern recognition and mode identification [e.g., 10–12]. For example, a deep learning technique has been adopted to reconstruct complex flow fields with sparse measurements [13]. However, ANNs rely heavily on nonconvex optimization and case-dependent training procedures affecting their generalizability. ANNs also share the same shortcoming as EMD, that it would be very hard to reach physical interpretations about the decomposition process and the resultant modes [14].

To address these limitations and to be able to instigate the transient response of a dynamic system, we explore the potential of the kernel mode decomposition (KMD) recently developed by Owhadi *et al.* [15]. KMD is a programmable network that can be interpreted equivalently from optimal recovering, Gaussian processes, or game theory settings. The network requires no training, and each module involved is interpretable and amenable to analysis. Through one-dimensional (1D) synthetic tests, Owhadi *et al.* demonstrated how KMD is capable of decomposing a complex noisy signal into the original modes with their varied amplitudes and frequencies accurate to machine precision. In the authors' previous paper [16], we inspected the effects of different network parameters on the KMD analysis results and demonstrated that with point-wise surface friction coefficient analyses, KMD can successfully identify different phases of the formation of a laminar separation bubble.

In this paper we extend KMD to achieve simultaneous localization in space and time domains. Three examples, including a synthetic case, a canonical flow case, and the formation process of an induced laminar separation bubble, are selected to explain the efficacy of the proposed framework. The main contributions of this paper are: (1) incorporate KMD into a sparsification analysis framework to enable space-time-frequency localization modal analysis, (2) inspect the formation process of a laminar separation bubble with the framework and successfully identify the two competing modes stemming from different mechanisms. Next, in Secs. II and III we introduce the basics of KMD with a 1D problem explaining how KMD can be used with a sparsification method and present a synthetic example to compare the results from the current method to some popular modal analysis methods. In Sec. IV a canonical two-sided oscillating lid-driven cavity flow is used to investigate the capability of the proposed KMD framework. The decomposition results and physical observations made about the formation process of a laminar separation bubble are presented in Sec. V. At the end of the paper, in Sec. VI, we conclude the current work and discuss possible future directions.

II. KERNEL MODE DECOMPOSITION

In this section we briefly introduce the KMD modular network developed by Owhadi *et al.* [15] and then discuss how to incorporate it into a framework to enable spatial analysis. Only the key components of KMD utilized in the current research will be reviewed, and the mathematical details of different modules are referred to the pioneered papers.

The structure of KMD for a sample signal is shown in Fig. 1. The input signal $v = \sum_i v_i$, as shown in the top-right panel, is composed of three coherent signals v_i, $i \in 1, 2, 3$, with varying frequencies and amplitudes in addition to a contaminating white noise v_4. The main aspect of KMD is to take a complex signal as the input and extract the essential modes by combining many fine modes from a mode bank that spans the spectral and temporal ranges of interest. For example, the shifted/scaled Gabor wavelets can be employed as a candidate of fine modes and formation of a
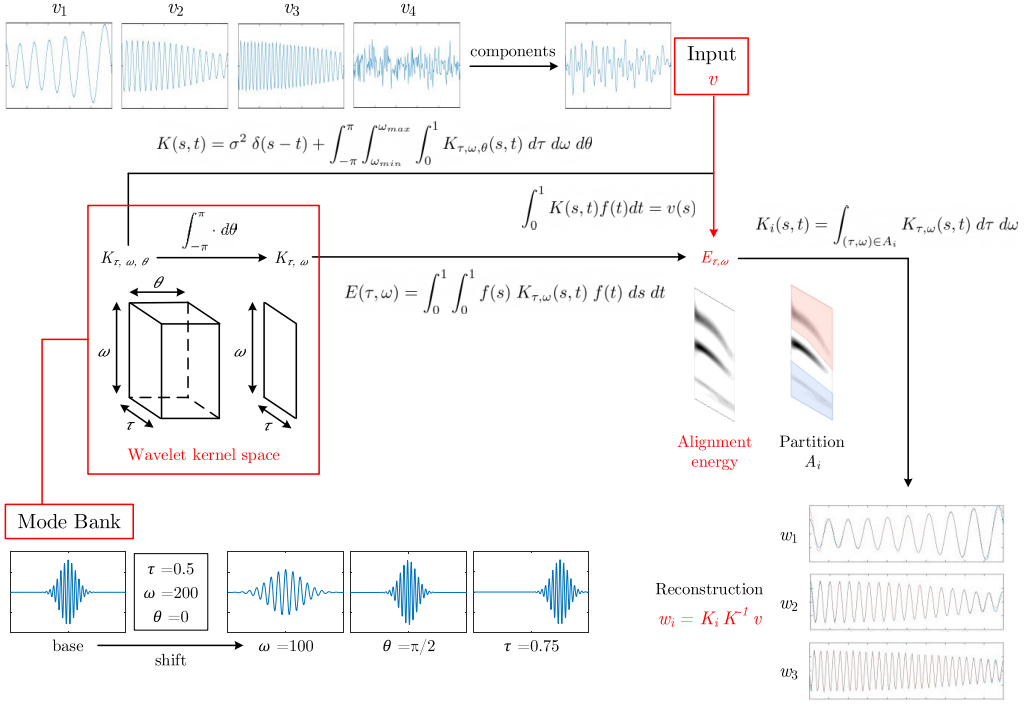
FIG. 1. Kernel mode decomposition procedure overview. In the reconstruction, the blue solid line is the original signal, and the orange broken line is the reconstruction from KMD.

mode bank,

$$\chi_{\tau,\omega,\theta}(t) = \left(\frac{2}{\pi^3}\right)^{1/4} \sqrt{\frac{\omega}{\alpha}} \, \cos\left(\omega(t-\tau)+\theta\right) \, \exp\left(\frac{\omega^2(t-\tau)^2}{\alpha^2}\right), \tag{1}$$

where the parameters τ, ω, and θ represent the delay time, frequency, and phase of the Gabor wavelets, respectively. The parameter α represents the width of the decaying envelope of the Gabor wavelets. The effects of modifying these parameters are shown in the top-left panel of Fig. 1. We adopted the notations used in [15] and name the first-level wavelet space as

$$\mathcal{I}^{(1)} = \{(\tau,\omega,\theta) \in [0,1] \times [\omega_{\min}, \omega_{\max}] \times (-\pi, \pi]\} \cup \{\sigma\}, \tag{2}$$

where σ represents the noise level.

The reproducing kernel of the corresponding Gabor wavelet $\chi_{\tau,\omega,\theta}$ is defined as the Mercer kernel (positive definite kernel) of

$$K_{\tau,\omega,\theta}(s,t) = \chi_{\tau,\omega,\theta}(s) \, \chi_{\tau,\omega,\theta}(t), \tag{3}$$

which stems from Mercer's theorem stating that the eigenfunction ϕ can be equivalently used to represent the action of any positive definite kernel function κ, or equivalently,

$$\kappa(x, x') = \sum_{i=1}^{\infty} \lambda_i \, \phi_i(x) \, \phi_i(x'). \tag{4}$$

The essential idea of KMD is to measure the alignment between the individual fine mode $\chi_{\tau,\omega,\theta}$ and the original signal v with their kernels. Assuming that the noise and the physical signal are

uncorrelated, the master kernel can be described as

$$K = K_u + K_\sigma, \tag{5}$$

where

$$K_u(s, t) = \int_{-\pi}^{\pi} \int_{\omega_{\min}}^{\omega_{\max}} \int_0^1 K_{\tau, \omega, \theta}(s, t) \, d\tau \, d\omega \, d\theta, \tag{6}$$

$$K_\sigma(s, t) = \sigma^2 \, \delta(s - t), \tag{7}$$

and σ quantifies the noise strength. Let f be the solution of the linear system

$$\int_0^1 K(t, s) f(s) ds = v(t), \tag{8}$$

which in the discrete setting is equivalent to

$$\mathbf{K}\mathbf{f} = \mathbf{v}. \tag{9}$$

Then an energy-based criterion can be defined as

$$E(\tau, \omega, \theta) = \int_0^1 \int_0^1 f(s) \, K_{\tau, \omega, \theta}(s, t) \, f(t) \, ds \, dt, \quad (\tau, \omega, \theta) \in [0, 1] \times [\omega_{\min}, \omega_{\max}] \times (-\pi, \pi], \tag{10}$$

where the variable E, as the energy of the optimal recovery map, is a measure of the alignment between the fine modes and the data. The variable E is called the "*alignment energy.*" The larger the alignment energy of a particular fine mode, the better that mode represents the data. In the following description we will alternatively adopt the discrete notation to explain the method for practical applications better.

Since our primary interest is to achieve time-frequency localization, we can reduce the wavelet space and collapse its phase dimension as

$$\mathcal{I}^{(2)} = \{(\tau, \omega) \in [0, 1] \times [\omega_{\min}, \omega_{\max}]\} \cup \{\sigma\}, \tag{11}$$

where the new reproducing kernel is characterized by

$$\mathbf{K}_{\tau, \omega} := \sum_{\theta \in (-\pi, \pi]} \mathbf{K}_{\tau, \omega, \theta}. \tag{12}$$

Equation (9) implies that

$$\mathbf{v}^T \mathbf{K}^{-1} \mathbf{v} = \mathbf{f}^T \mathbf{K} \mathbf{f}, \tag{13}$$

and it follows that

$$\mathbf{v}^T \mathbf{K}^{-1} \mathbf{v} = \sum_{\omega \in [\omega_{\max}, \omega_{\min}]} \sum_{\tau \in [0, 1]} \mathbf{E}(\tau, \omega) + \mathbf{f}^T \mathbf{K}_\sigma f, \tag{14}$$

where $\mathbf{E}(\tau, \omega) = \sum_{s \in [0, 1]} \sum_{t \in [0, 1]} \mathbf{f}(s) \mathbf{K}_{\tau, \omega}(s, t) \mathbf{f}(t)$ is the alignment energy in the time-frequency domain. Equation (14) suggests that by partitioning the kernels with the information learned from the alignment energy $\mathbf{E}(\tau, \omega)$, we can recover the optimal reconstructions of the coherent parts of the input signal. In the 1D example (Fig. 1), we can partition the time-frequency domain into three separate subsets based on E, essentially identifying the number of modes included. If the subspaces of the time-frequency domain are identified as A_i, $i \in 1, 2, 3$, then the kernel associated with the coherent mode i is

$$\mathbf{K}_i(s, t) = \sum_{(\tau, \omega) \in A_i} \mathbf{K}_{\tau, \omega}(s, t). \tag{15}$$

From the optimal recovery theorem, we can then extract the coherent modes through

$$\mathbf{w}_i = \mathbf{K}_i\,\mathbf{f}. \tag{16}$$

Note that $\mathbf{w}_i = \mathbf{K}_i\mathbf{f} = \mathbf{K}_i\mathbf{K}^{-1}\mathbf{v}$ can be interpreted as a projection operation—finding the fine modes that are most aligned with the distinct components of the input. In Fig. 1 we show how KMD perfectly recovers the three modes up to machine precision with this procedure. There are multiple ways to decide the instantaneous frequencies of the modes, and we adopted the definition [15] of

$$\omega_i^e\,(t) = \operatorname{argmax}_{\omega:(t,\omega)\in A_i}\,\mathbf{E}(t,\omega). \tag{17}$$

In this section, we briefly introduce the essential modules of implementing KMD for transitional mode extraction. To summarize, KMD utilizes the reproducing kernel and the subsequently derived alignment energy to determine which fine modes in the mode bank best align with the input signal and reconstruct the input signal. KMD can be viewed as a network due to its composition of connected customizable modules. The mode banks can be viewed as multiple nodes interacting with each other based on the similarity to the original signal and the grouping of the temporal and spectral properties. The higher the alignment energy a node possesses, the more influence it has in the network. In other words, the particular node (fine mode) with higher alignment energy represents the behavior of the system better. The KMD network is also easily programmable and highly customizable. The programmable nature of KMD lies in the base mode bank choice, along with the grouping and similarity filter. The similarity is characterized by the alignment energy, which is used to pool the fine modes and aggregate them to recover the principal components of the original signal. This pooling operation can be chosen based on the users' requirements, methods such as thresholding or graph cut are proposed. Furthermore, the fine modes can also be high dimensional, nontrigonometric, or even self-adaptive. Some might wonder what the difference is between KMD and wavelet decomposition [17]. In this current setting, the differences between the two methods do not seem very obvious; both serve as a pattern recognition problem with wavelets as the basis, and both are multiresolution analyses that can deal with transitioning signals. However, KMD is a modular network that is highly flexible. The mode bank can be any mode shape, from sinusoidal to triangular wave. Advanced modules designed for handling crossing frequencies, vanishing modes, or an unknown wave-form basis can be readily deployed to handle more complex problems. Also, the alignment energy as a by-product of the procedure offers a convenient energylike criterion to classify how well each fine mode represents the input signal. As a regression operation, every step of the process stays linear except for the ancestor-descendent relation identification, which is user definable and could be interpretable. These benefits make KMD an ideal modal analysis tool for complex dynamic systems with the transient response, with each step being amenable to analysis. In this manuscript we would like to focus on testing this network-based method on complex transient flow problems, so we chose the wavelets as our base wave form. With this choice of base mode, the KMD on the surface shares similarities with the wavelet transform, but the underlying network operates in a comprehensive way with a lot of potential for expansion tailored to users' needs. In the next section we extend KMD with a spatial analysis framework that utilizes the alignment energy as a clustering criterion.

III. SPACE-TIME-FREQUENCY LOCALIZATION WITH A SPARSIFICATION KMD FRAMEWORK

To expand KMD into an extra dimension of space for space-time-frequency localization, an intuitive approach is using two- and three-dimensional (2D, 3D) wavelets to form the mode bank. For example, for 2D kernels, instead of using $K_{\tau,\omega,\theta}$ we now have $K_{\tau,\omega,\theta,x,y,\alpha_x,\alpha_y}$, where (x,y) is the center of the 2D wavelets, and α_x and α_y are the width of spatial decaying in x and y direction, respectively. The extra parameters describe the spatial distribution, and enough resolution has to be considered to recover the locations where rich dynamics are present. In practice, this increases the computational complexity by several orders and renders the computation of the
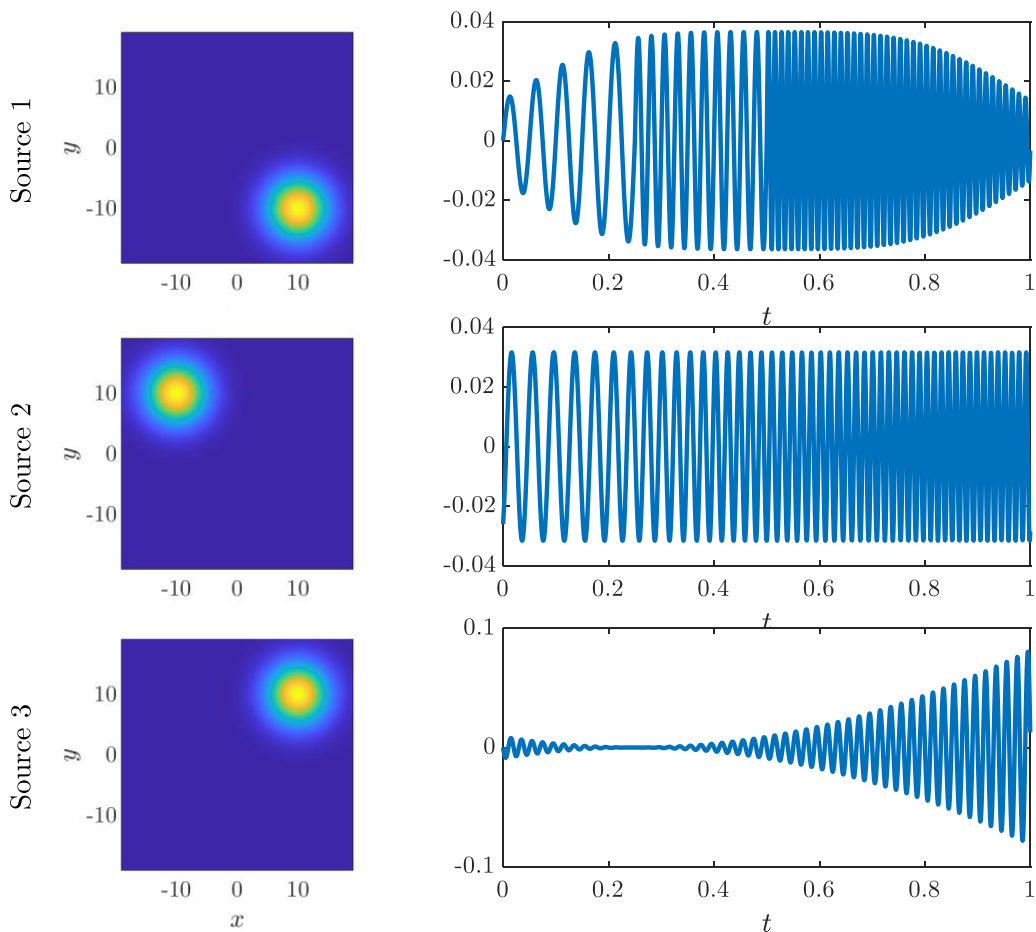
FIG. 2. Spatial distributions and temporal amplitudes of the synthetic case.

kernels impractical. To address this challenge, we adopted the idea of spatial clustering with the alignment energy. We will first describe the synthetic data set used to showcase the framework, perform two popular modal analysis methods, POD and mPOD, on the data set, and then show how the KMD framework can extract accurate modal information in both spatial and temporal domains.

The synthetic test case consists of three orthogonal pulsing Gaussian distributions; their locations and amplitude time histories are shown in Fig. 2. The spatial domain is discretized into a uniformly distributed Cartesian grid with a dimension of 256×256 points over a domain of $x \in [-20, 20]$, $y \in [-20, 20]$. The temporal domain is divided into 2000 equally spaced intervals in the span of $t = [0, 1]$. All three sources consist of Gaussian distributions with spatial standard deviations of $\alpha = 5$, and the strength of the three sources

$$S_1(\tau) = N_1 \ \sin(2\pi f_1 \tau) \ \exp[-16(\tau - 0.5)^4], \tag{18}$$

$$S_2(\tau) = N_2 \ \sin(2\pi f_2 \tau), \tag{19}$$

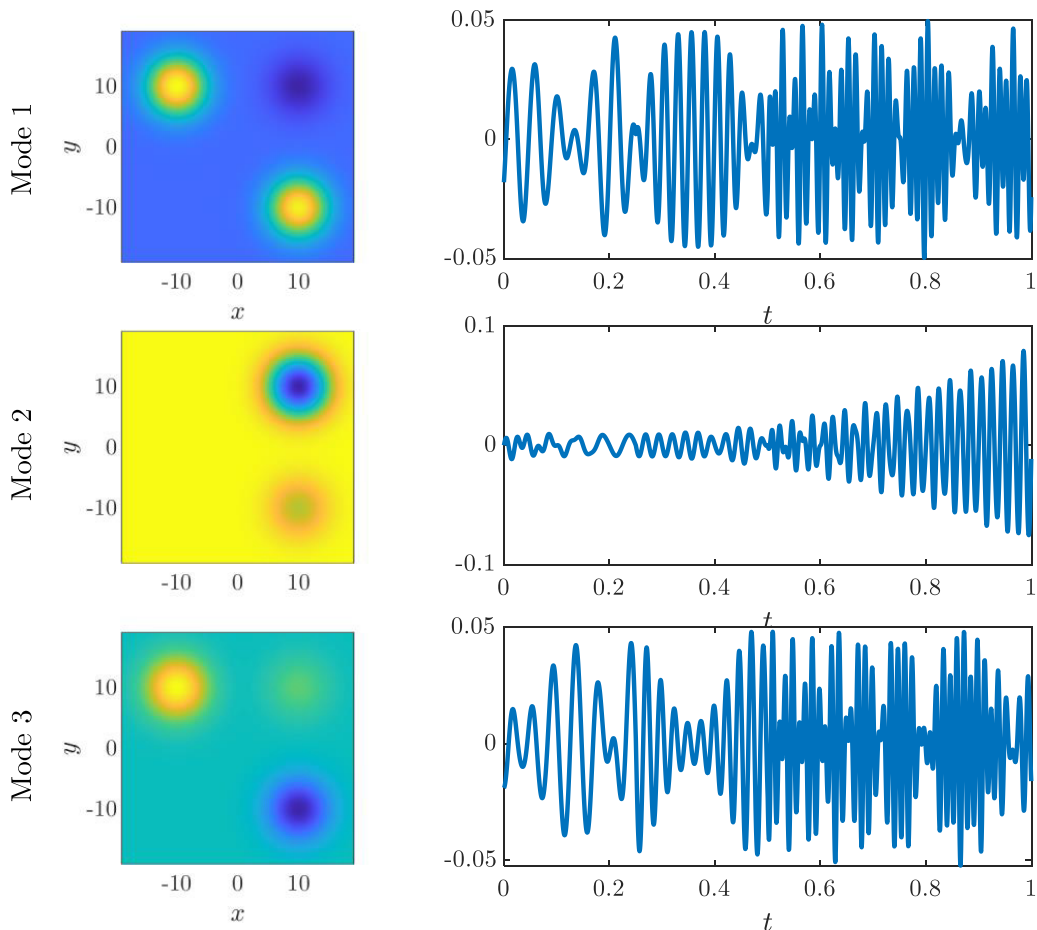$$S_3(\tau) = N_3 \ \sin(2\pi f_3 \tau) \ (\tau - 0.5)^2. \tag{20}$$

FIG. 3. The three leading POD modes and their corresponding temporal content of the synthetic case.

The first source is located at $(x_1, y_1) = (10, -10)$ and has an instantaneous frequency of $f_1 = \{20, t \in [0, 0.25]; 40, t \in (0.25, 0.5]; 80, t \in (0.5, 1]\}$, with a smooth square box modulation in the temporal envelope. The second source, located at $(x_2, y_2) = (-10, 10)$, has a frequency profile f_2 that linearly increases from 25 to 75 and a constant amplitude. The third source centers at $(x_3, y_3) = (10, 10)$ and has a parabolic temporal amplitude envelope with the frequency fixed at $f_3 = 50$. The weightings N_k, $k \in \{1, 2, 3\}$ normalize the three sources with their corresponding norms across the time span so all signals have similar integrated intensity. The frequency trajectories of the input signals are shown later in Fig. 7(b). The data set is designed so that the three modes are mostly uncorrelated spatially but share similar energy and have crossing frequencies. Two modal analysis methods will be used to instigate this system as a reference problem.

The data $S = S_1 + S_2 + S_3$ is reshaped into the data matrix $\mathbf{D}$ with the dimension of 65536×2000. The first method deployed is the classical snapshot proper orthogonal decomposition (POD) [18,19]. In practice, this method is equivalent to executing a singular value decomposition (SVD) on the data matrix, with the columns of the left singular matrix containing the spatial POD modes $\boldsymbol{\phi}_j$ and the singular values λ_j representing the energy of the modes. The temporal coefficients of the modes can be acquired from projection $a_j = \mathbf{D}^T \boldsymbol{\phi}_j$. Shown in Fig. 3 are the first three most
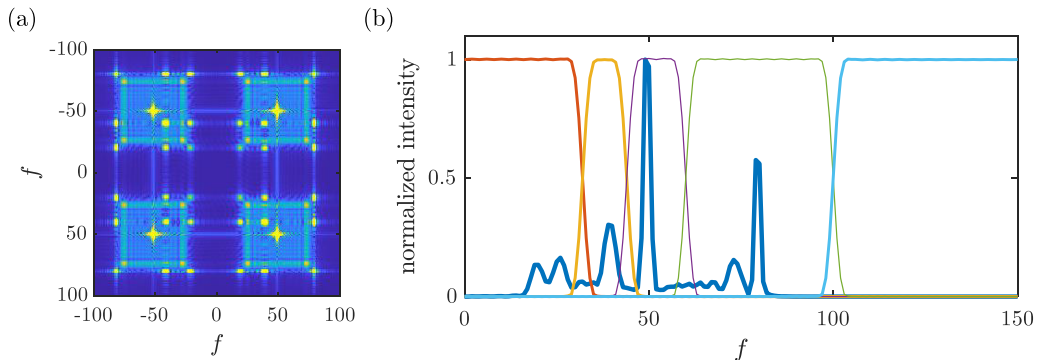
FIG. 4. The (a) discrete Fourier transform of the data matrix and (b) filter design based on the spectral peak identified from the diagonals of the Fourier transformed data.

energetic modes and their corresponding temporal structures. The biggest downfall of the POD method, which is the spectral mixing, can be clearly observed here. Although the three modes can capture the locations of the sources accurately, due to the similar frequency and amplitude, POD fails to effectively differentiate the three disjoint modes. We can observe from the spatial distributions that in all three leading modes, three sources present together, the temporal envelopes do not reflect the shape of the original signals, and the frequencies do not have a smooth transition and a lot of mixing happens, especially when the frequencies of different sources approach each other.

The second method deployed is the multiscale POD (mPOD) developed by Mendez *et al*. [2], which has been applied to different fluid problems [20,21]. This method aims to solve the spectral mixing of POD by filtering the data set. The data matrix is transformed into spectral space and then filtered based on the observed spectrum with a low-pass filter, a high-pass filter, and a series of nonoverlapping bandpass filters spanning the whole spectral domain. Each filter is designed to include a single identified spectrum peak of the transformed data matrix D. We show an example of the discrete Fourier transformation of the current data matrix, the spectrum of its diagonal, and the filter designed based on the spectral peak in Fig. 4. This operation is equivalent to isolating the contribution of dynamics with distinct frequencies in the temporal domain. POD is then applied to each partition to extract the energetically dominant modes in each partition, which should now have a much cleaner spectral content. The results of mPOD are demonstrated in Fig. 5, with the leading mode of the three partitions covering the spectral range of $f = [0, 32], [32, 48], [48, 160)$, respectively. It can be observed that a good separation of the spatial distributions is identified, and in the spectral domain, we can see that the three modes do not suffer much from spectral mixing, and instead, consistent frequencies are identified for each mode. However, when a large frequency shift happens, mPOD cannot track the spectral trajectory as it is limited to the filter-designed frequency range.

Besides the results shown for POD and mPOD, many other state-of-the-art modal analyses cannot be employed as a global modal analysis method for systems consisting of multiple local modes with crossing frequencies and similar energy contents. Although not shown here, another popular modal analysis method, the dynamic mode decomposition (DMD), could not exactly extract the three component modes similar to mPOD, as DMD produces only single-frequency modes. Hence, a framework based on the KMD is proposed to address these types of responses. The procedure of applying this framework to the current example is shown in Fig. 6. A series of operations are linked to accomplishing spatial KMD analysis, starting with performing KMD on sparse spatial locations. The process is fully parallel and independent for each mode. In this example, on each grid point the alignment energy intensities of the leading frequencies [identified with Eq. (17)] are calculated and collected into the spatial intensity plot. An important assumption
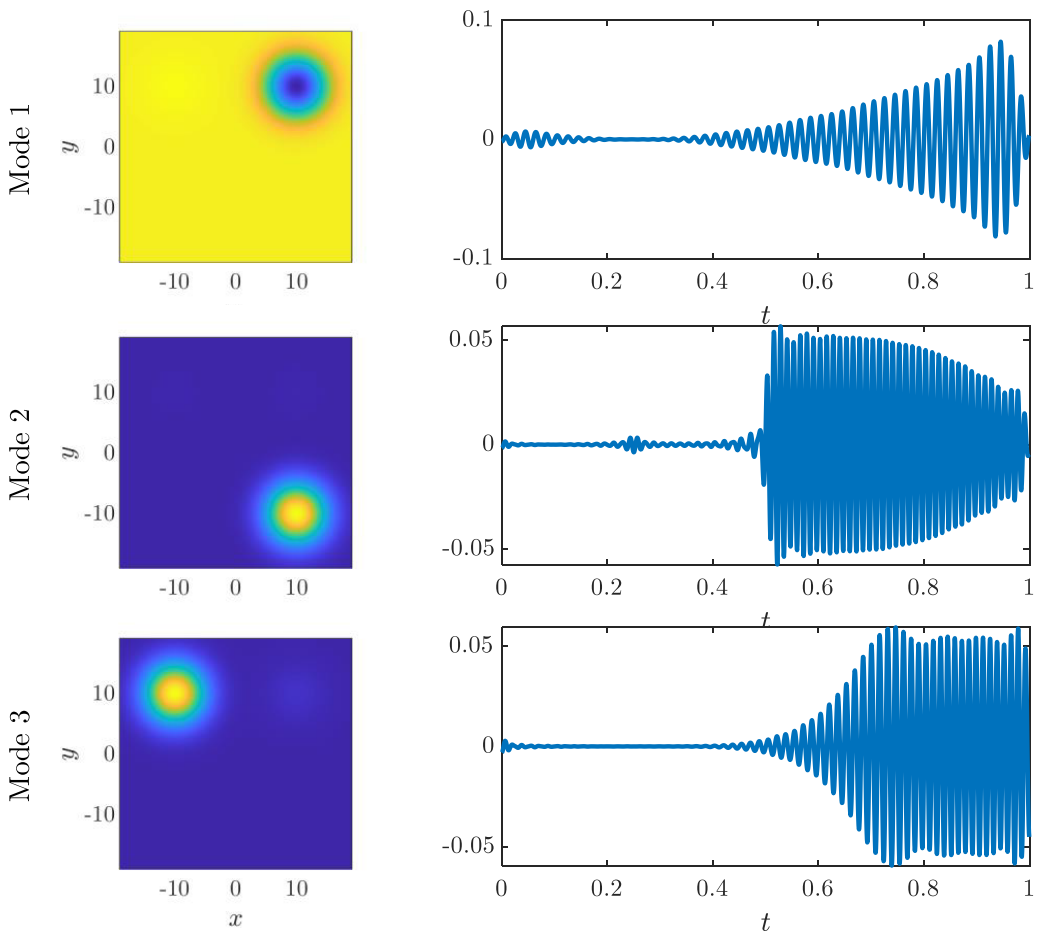
FIG. 5. The three leading mPOD modes and their corresponding temporal content of the synthetic case.

is implicitly made here: points with similar intensity in close spatial proximity should bear similar frequency contents, since the same set of mode banks is used to find the alignment energy. They are then categorized into the same spatial feature. Likewise, if the leading frequency is similar in temporal proximity, we can assume that these points belong to the same continuous flow feature. Note that these implications infer that the interested system has dynamics that are continuous in both space and time, such as incompressible flow phenomena. Hence we can utilize the alignment energy for spatial and temporal clustering to identify flow features in later sections.

As Fig. 6 shows, the collected alignment energy over a chosen threshold is first clustered in space within each frame. The intensity histogram is used to determine the number of clusters, then the frequency of the centroid of each cluster is used to match with the cluster in the subsequent frames to ensure temporal continuation. This process follows the same philosophy of KMD, sparsifying the spatial and temporal data and then recombining them based on physically interpretable operations. This framework results in a space-time-frequency localization modal decomposition, as shown in Fig. 7. The clustering successfully identifies three different sources, and we can collect the frequencies of their centroids. With the frequencies available, we can partition the alignment energy and reconstruct the temporal amplitudes with Eq. (16). We can see that the three sources are fully
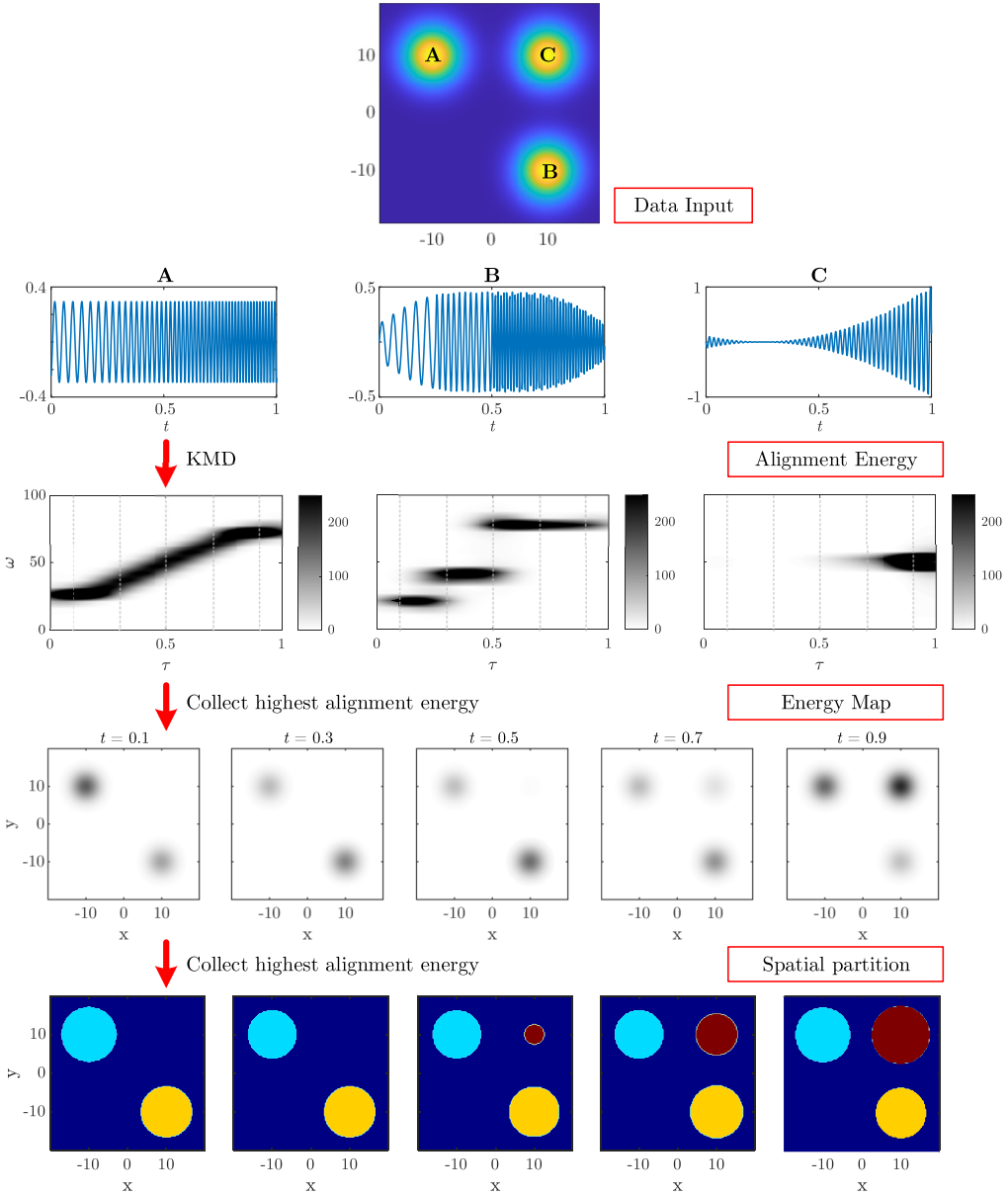
FIG. 6. Procedure of applying the KMD sparsification framework to the synthetic case.

isolated spatially and their corresponding frequencies are also captured, demonstrating how well this KMD sparsification framework works. Since we assign a threshold to the alignment energy, mode 3 does not appear until its intensity is sufficiently large. Note that for source 1 (the yellow curve identified), the frequency transitions follow a multistep function. Statistically, when the behavior of a signal changes very fast it should be treated as separate signals, but here they are the same color for their representation to highlight how well KMD works and track the change. Compared to POD, which suffers from spectral mixing, and mPOD, which could not differentiate modes separated in space with similar frequency contents, the KMD framework can identify essential modes even when
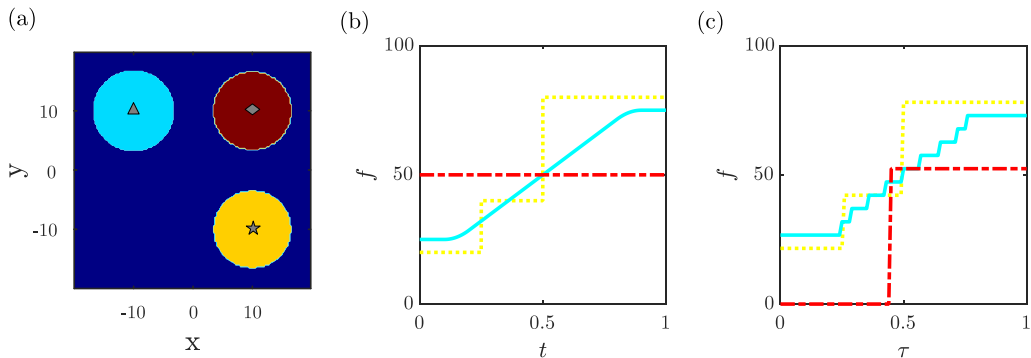
FIG. 7. (a) The spatial distribution of the three identified clusters, (b) their original frequencies, and (c) the identified frequencies with the KMD framework (triangle-yellow dotted line, circle-red broken line, and star-cyan solid line).

they vary over time. The capability of the proposed framework will be further demonstrated in the following sections.

IV. TWO-SIDED OSCILLATING LID-DRIVEN CAVITY FLOW

In this section we show another example of a two-sided lid-driven cavity flow to demonstrate the applicability of KMD framework to form reduced-order representation of dynamical systems. The problem setup, shown in Fig. 8(a), consists of oscillating top and bottom panels and two stationary sidewalls. Lid-driven flow is commonly used as a benchmark problem for the computational fluid dynamics solver [22], mostly with a moving panel traveling at a constant speed. In heat transfer problems, the two-sided moving walls are proven helpful in the heat mixture [23], and the moving velocity and direction significantly alter the mixing efficiency. Recently, Bhopalam *et al.* [24] focused on two-sided oscillating lid-driven cavity flow by systematically changing the Reynolds number (Re), oscillating frequency($\tilde{\omega}$), and speed ratio (SR) between the two moving walls and showed that while Re and $\tilde{\omega}$ affect the fluid penetration depth, SR controls the size and strength of the additional vortices. So far, the research on the two-sided lid-driven flow has mostly been confined to constant wall velocity or moving walls in which the oscillating frequency and amplitude stay constant. Here we will explore how the KMD framework can reveal the dynamics when the two walls oscillate at varying frequencies and amplitudes.

In this example we adopt a vorticity–stream function formulation to conduct numerical simulation [25]. A square domain with width $L = 1$ is discretized into a Cartesian grid with the dimension of $(N_x, N_y) = (256, 256)$. The boundaries are all impenetrable (normal velocity $v_N = 0$), and no-slip conditions are applied. The top and bottom panels oscillate with velocities u_{top} and u_{bot} with smoothly varying frequencies and amplitudes, shown in Figs. 8(b) and 8(c). Note that the average amplitudes of the velocity of both panels are $A = 1$, and the Reynolds number of the system defined with the average panel velocity amplitude and the cavity width is Re $\equiv AL/\mu = 1000$. Figure 9 shows the streamlines of some snapshots at different moments. It can be seen that as the frequencies and amplitudes change, rich dynamics can occur. At first, when the oscillation frequencies of both panels are higher, the vortices induced by the shear effects stay relatively close to the panel and there is less interaction between the two sets (top and bottom) of vortices. As the frequencies of the panels decrease, the vortices become larger and start to cross the midsection of the cavity. As the top panel oscillation amplitude decreases and the bottom panel oscillation amplitude increases, the bottom vortices infiltrate deep into the cavity and interact with the top vortices. When the panel frequencies change at $t > 200$, the slow- and large-amplitude oscillation of the bottom panel creates a large circulation that occupies most of the domain. With the oscillation frequency and amplitude variation,
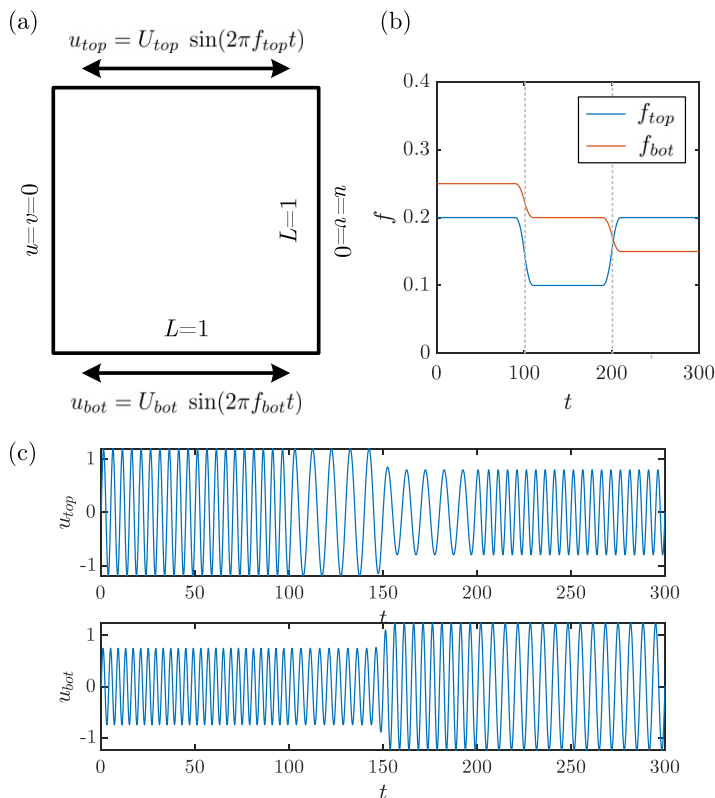
FIG. 8. (a) The setup of the two-sided oscillating lid-driven flow problem, (b) frequencies of the two panels, and (c) the velocity trajectories of the two panels.

the cavity flow expresses transient flow evolution, which is difficult for the classical global modal decomposition method to track. As an example, the leading mPOD modes shown in Fig. 10 exhibit the limitation of the classical global modal analysis when facing this kind of system: although the DFT results return clear peaks of the spectrum, the nonuniform energy distribution in the domain
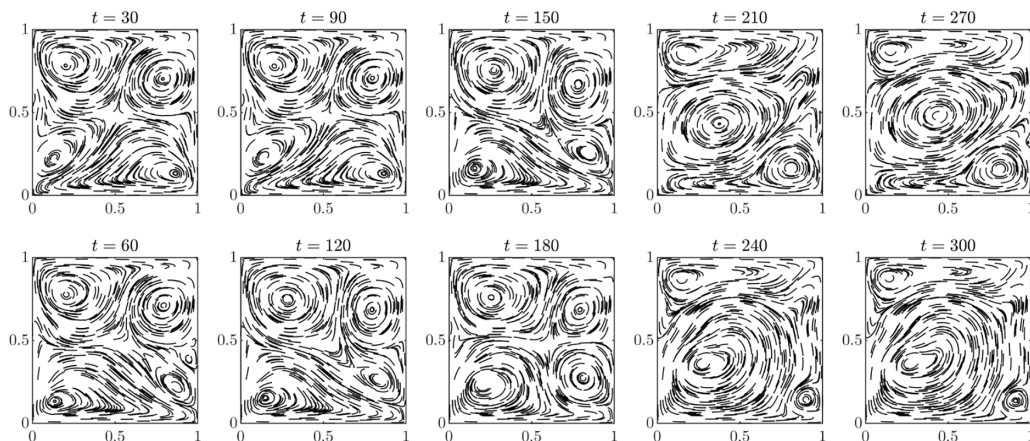

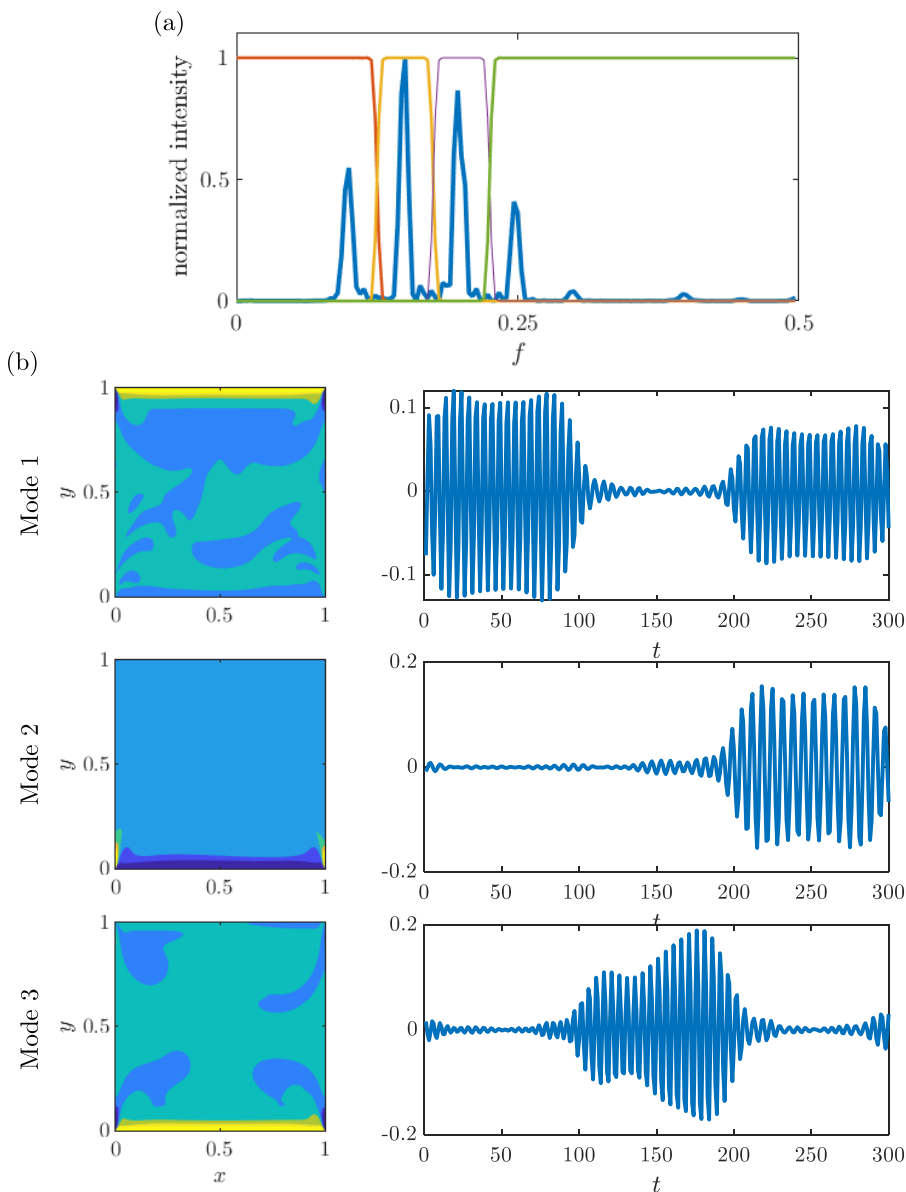FIG. 9. Snapshots of the streamline of the two-sided oscillating lid-driven flow.

FIG. 10. (a) The diagonal elements of the discrete Fourier transformed data matrix and the linear filter, and (b) the three leading mPOD modes and their corresponding temporal content of the two-sided oscillating lid-driven flow.

and the transitioning of the system dynamics prevent the continuous space-time tracking of the flow features. Specifically, despite capturing the $f = 0.2$ frequencies at the right temporal moment in mode 1, the mode shape could not reflect when the top or bottom panel is actuated; mode 2 could not capture the vortices associated with the $f = 0.15$ bottom panel oscillation since the flow close to the panel contains way higher energy. With its capability of locally extracting frequencies and relative intensity in the form of alignment energy, the proposed KMD sparsification framework could better instigate the underlying dynamics of these kinds of systems.
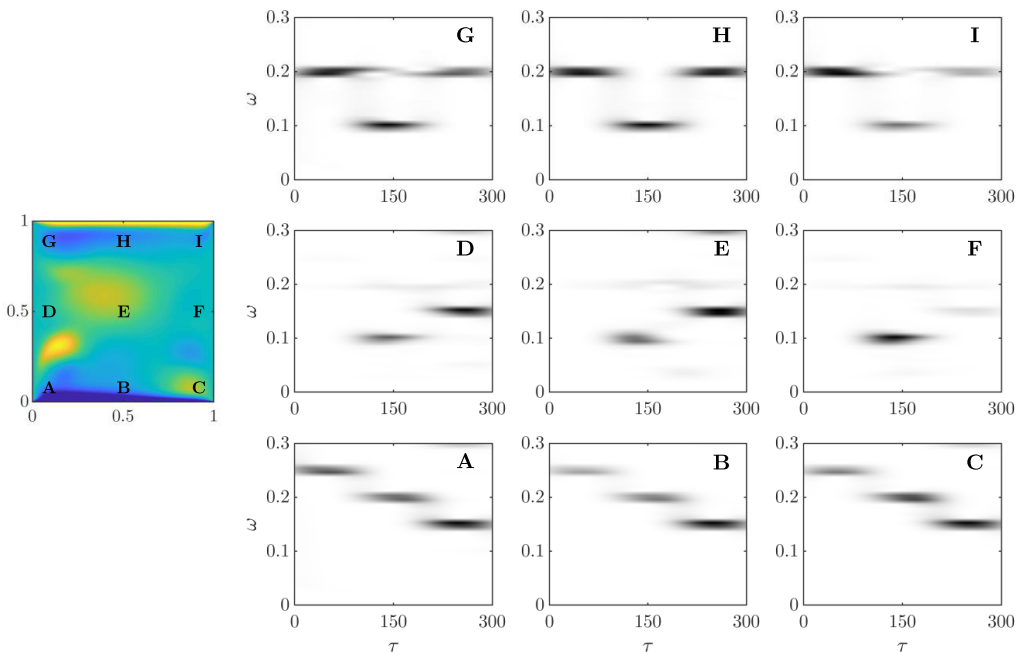
FIG. 11. The alignment energy in the time-frequency domain at different locations in the cavity.

Figure 11 shows the vorticity alignment energy at different locations in the flow. We can see that closer to the two panels, the identified frequencies are similar to that of the panel oscillation. This is reasonable, as the vortices shed due to the shear effect have the strongest connection to the panel. Further into the cavity, for example, at locations denoted as points **D**, **E**, **F**, only for $t > 100$, there are stronger alignment energy contents. This in part coincides with our previous observation from the streamlines that only when the panel frequencies decrease, the flow in the middle region is perturbed. Also, contrary to the region close to the panel where mostly only one dominant frequency is observed at a time, in the center of the domain, multiple frequencies are identified. This indicates that both panels are affecting the flow field at the same time. We can take these identified frequencies, extract their alignment energy intensity individually, and collect them to corresponding intensity maps.

Figure 12 shows the evolution of these alignment energy maps. There are four dominant frequencies throughout the temporal sequence: $f = \{0.1, 0.15, 0.2, 0.25\}$. Since the alignment energy tracks the locally harmonic components, we do not see the individual vortices but vortical "fingers" that indicate how far the vortices reach within the domain. In the early stage, $t < 100$, when the top panel moves at $f = 0.2$, we see that there are vortex fingers oscillating with the corresponding frequency $f = 0.2$ and the subharmonic mode $f = 0.1$. When $t > 100$, we see that the slow panel movement induces more elongated structures that fill the middle part of the cavity. The $f = 0.15$ has a few harmonic modes at first, but once the bottom panel starts to move at this frequency with a large amplitude, the vortical finger-type structures quickly extend into the domain and eventually touch the top panel. Notably, in this mode a nonsymmetrical distribution is identified. This only happens when the penetration depth is large enough to sense the phase difference between the two sources, the bottom and top panels. The two panels oscillate out-of-phase, and the vortices created do not meet in the middle but push each other to the side and create the antisymmetric shuriken-shaped flow field. The $f = 0.25$ mode is relatively uneventful, with a small penetration depth, and does not interact with other parts of the flow. This mode disappears immediately after there is no panel movement at this specific frequency. In contrast, for the $f = 0.2$ mode, rich dynamics can be seen
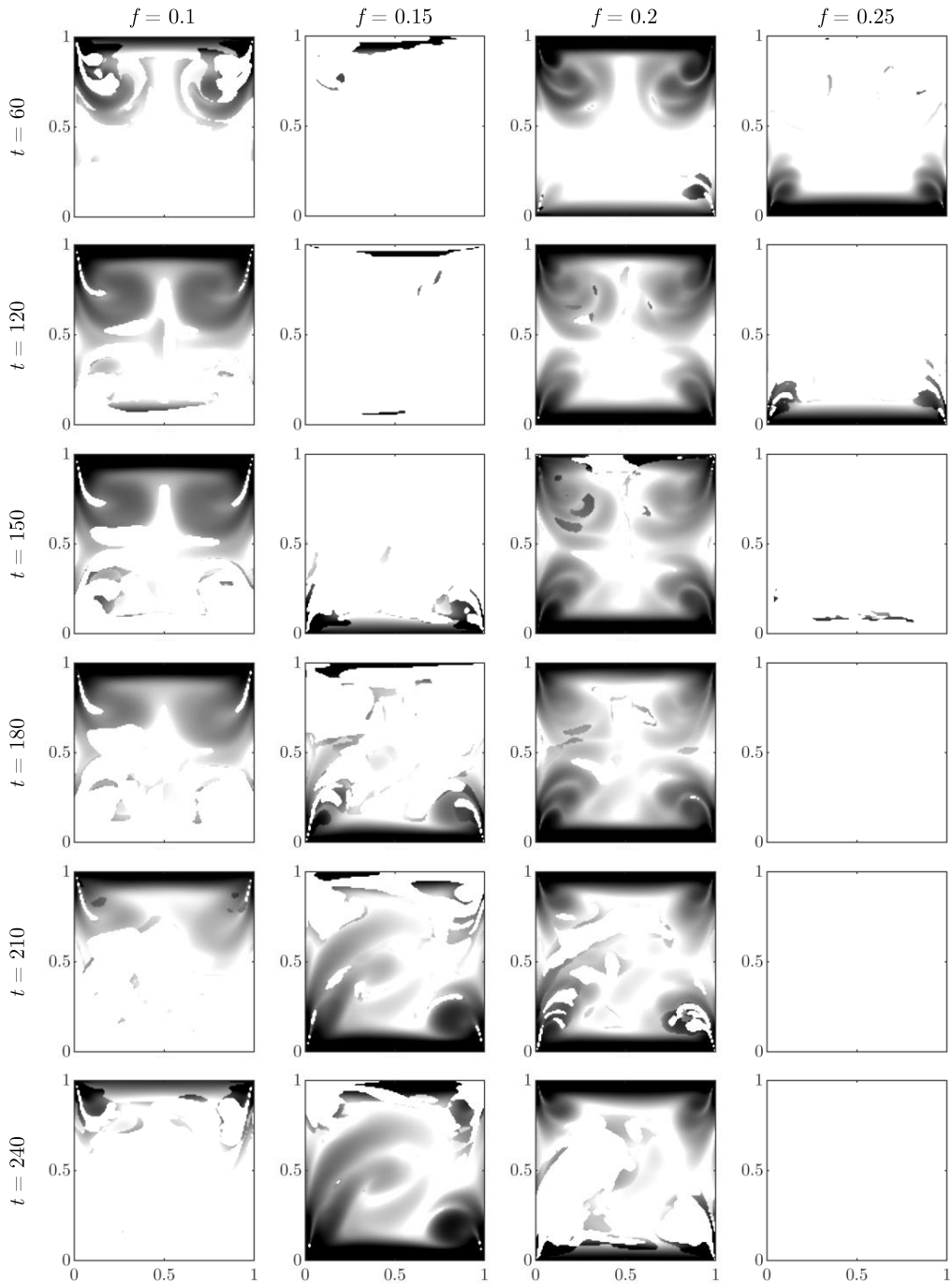
FIG. 12. The evolution of the alignment energy maps of the two-sided oscillating lid-driven flow.

when both the top and bottom panel move at this frequency. It can be seen that at the early stage, $t = 60$, two strong vortices form close to the top panel; then as the bottom panel changes its motion to $f = 0.2$ at $t > 100$, vortical fingers start to extend upward from the bottom surface. The top
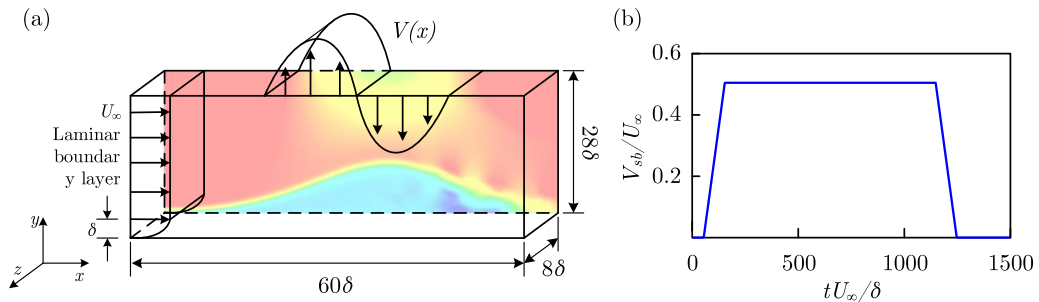
FIG. 13. (a) Schematic of the computational setup and (b) the amplitude of the suction and/or blowing boundary condition.

vortex pairs are now related to the superharmonics of the $f = 0.1$ panel motion. When the top panel returns to its oscillation with $f = 0.2$, the penetration depth becomes a lot smaller. Two mechanisms contribute to this: one is that the panel oscillation amplitude is smaller now, and the other is that the strong vortices form from the bottom panel motion suppress the development of the vortices at the top panel. We can also see when $t = 240$ the $f = 0.2$ mode is also nonsymmetrical where the left side is compressed by the large $f = 0.15$ finger.

Overall, with the use of the alignment energy, we could successfully isolate different spectral contents locally in both space and time through the sparsified KMD network. The alignment energy map provides a deeper understanding of the system in terms of flow feature localization. While the previous synthetic example demonstrates how the framework can isolate modes with crossing frequencies and disjointed spatial distribution, here we further show how to track the transient moving and deforming flow features. Next we will apply the KMD framework to a practical engineering problem to explore how it can help us understand the physics of complex flows.

V. FORMATION OF A LAMINAR SEPARATION BUBBLE

In the previous sections the applicability of the KMD framework for space-time-frequency localization is demonstrated through synthetic and canonical test cases. We now apply this method to the formation process of a laminar separation bubble as a sample model for a vast group of related engineering problems. The setup of the numerical simulation is explained in detail in [16], and only a brief introduction is present here.

Figure 13(a) shows the schematic of a separation bubble induced through suction/blowing (s/b) boundary conditions on a top flat boundary [26]. The vertical velocity profile of the top surface is described by [27]

$$V(x) = -V_{s/b}(t) \; \sin\left(\frac{2\pi(x - x_s)}{L_s}\right) \; \exp\left[-a_s\left(\frac{2(x - x_s)}{L_s}\right)^{b_s}\right], \qquad (21)$$

where $V_{s/b}$ is the peak amplitude of suction and blowing, and x_s, a_s, and b_s are parameters of the spatial distribution. A zero vorticity condition is enforced on the top boundary to determine the streamwise velocity boundary condition. The s/b amplitude V_s/b rises from zero and plateaus at a specified value before dropping back to zero as shown in Fig. 13(b). This profile can be viewed as a simplified model for a gust passing through a foil. An incompressible flow solver [28] is used to perform the numerical simulation. The freestream velocity U_∞ and boundary-layer thickness δ at the leading inlet are used as the characteristic velocity and length scales. Based on the experimental results [29], the Reynolds number based on the boundary layer thickness is set as $\mathrm{Re}_\delta = 865$. Figure 14 demonstrates the time history of spanwise-averaged streamwise velocity during the time interval in which the previously shown s/b boundary condition changes. The colormap of these
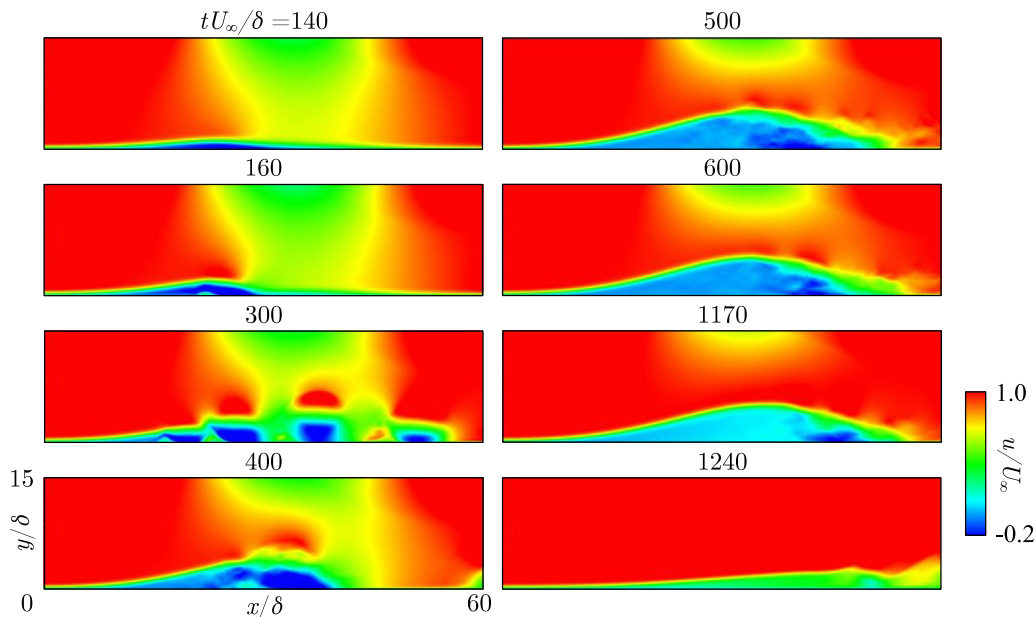
FIG. 14. Snapshots of the streamwise velocity of the formation of a separation bubble subject to unsteady flow condition shown in Fig. 13(b).

snapshots is adjusted so that the color blue indicates reverse flow. It is observed that there are three major phases in the bubble formation process: a small separation bubble forms first; then as the s/b intensity reaches its high-amplitude plateau, a series of roll-up vortices dominate the flow; and finally, a large separation bubble with a shear layer develops. We will now apply the proposed KMD framework to dissect this formation process, focusing on the temporal period of $tU_\infty/\delta = [100, 650]$, which starts from the rising of $V_{s/b}$ until after the separation bubble is fully established, to pinpoint the onset of these different phases.

Figure 15 shows the process of the KMD sparsification network. Here we use the time derivative of the vorticity as the input. Three points are plotted to show the transient responses in different parts of the flow. The alignment energy is calculated and collected into the alignment energy intensity map. Six different clusters are found to be sufficient to classify the observed transient behavior as shown plotted in Fig. 16(a). Note that some of these clusters have transitioning frequencies and they can also shift in space. We selected three representative clusters and showed their leading frequencies over time in Fig. 16(c). Two separate distinct behaviors with different frequencies are observed in clusters 3 and 5. Cluster 3 represents the onset of the roll-up phase, appearing right at the start when the s/b is turned on. It is located directly below the point on the top boundary where the largest suction strength occurs. The frequency of this cluster coincides with the roll-up vortices frequencies obtained from applying FFT to the surface friction (C_f), shown in Fig. 16(b) at location $x/\delta = 45$ [16]. Interestingly, this mode disappears shortly after the s/b strength flattens at the maximum value. This implies that the roll-up vortices phase is supported by the *increase* of the s/b strength, which creates a larger pressure gradient that forces the separation bubble shed away from the surface and results in the convective vortex structure, akin to how the vortex shed from the leading edge of an upward pitching airfoil.

On the other hand, the frequency of cluster 5 matches to what is identified from the C_f plot at the shear layer attachment point and captures the shear instability in the system. An interesting observation is that while we anticipate the shear layer to only appear after the separation bubble is established, with the KMD framework, we found that this mode exists much sooner than the
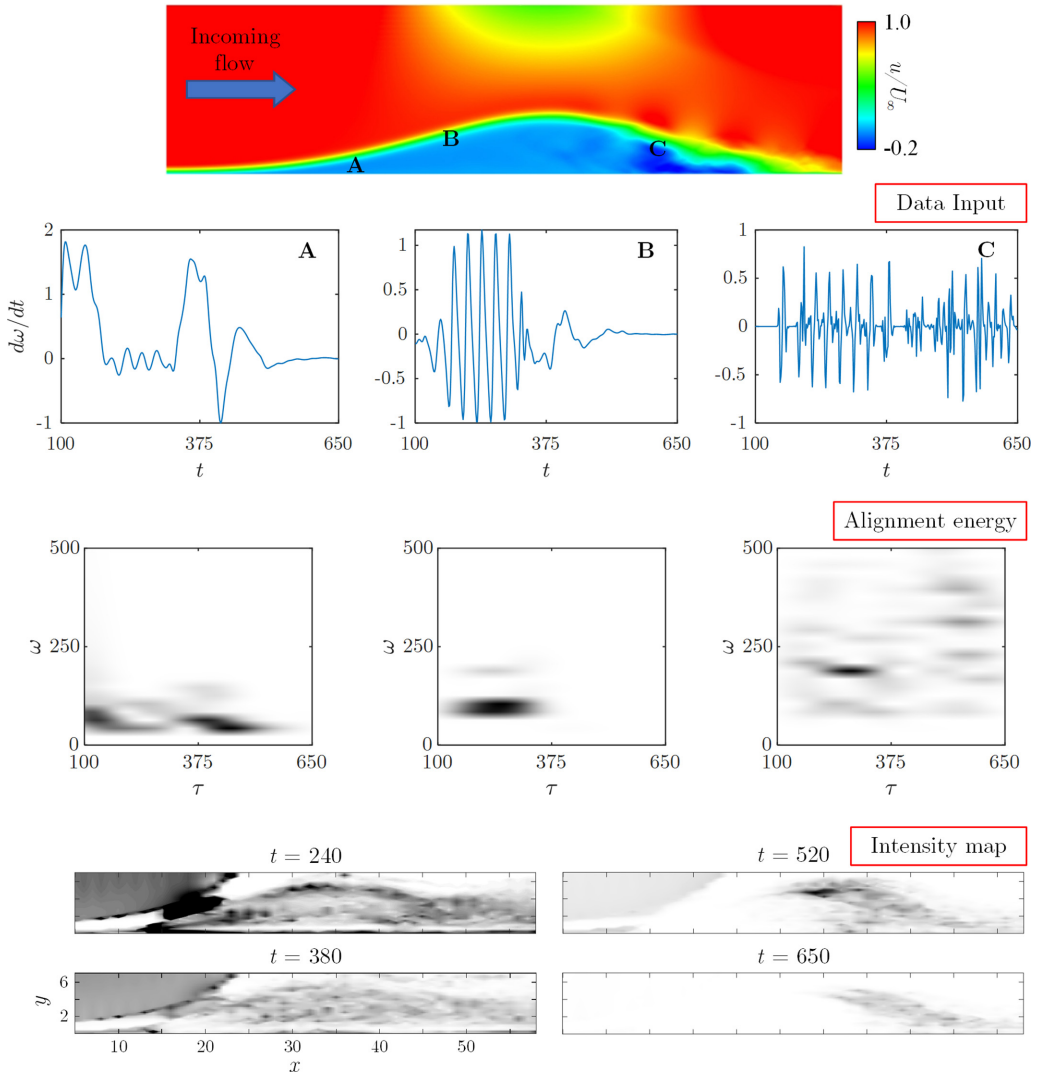
FIG. 15. KMD procedure applied to the formation process of a laminar separation bubble.

formation of the bubble. The shear layer mode, in fact, appears shortly after the s/b strength rises to a certain threshold level and continues to be at the interface of the suction and blowing afterward. As the roll-up vortices diminish after the s/b strength plateaus, the centroid of the shear layer cluster gradually shifts toward the downstream. The starting point of the occupied region of this mode is also observed to be close to the transitioning point between the suction and blowing parts of the top boundary. This implies that the shear layer is supported by the shear effect between the opposite velocity direction of suction and blowing actuation, along with the Kelvin-Helmholtz instability created from the velocity difference between the free stream and the reverse flow inside the separation bubble. For feature 4, we see that these two modes, the roll-up vortices induced by the increasing of s/b strength, and the shear layer supported by the velocity difference at the s/b interface compete with each other. The leading modes based on the KMD intensity alternate until the large separation bubble is settled. Once the s/b strength plateaus, the roll-up vortices continue to be formed over a few more cycles, but since the source of this phenomenon diminishes, it eventually
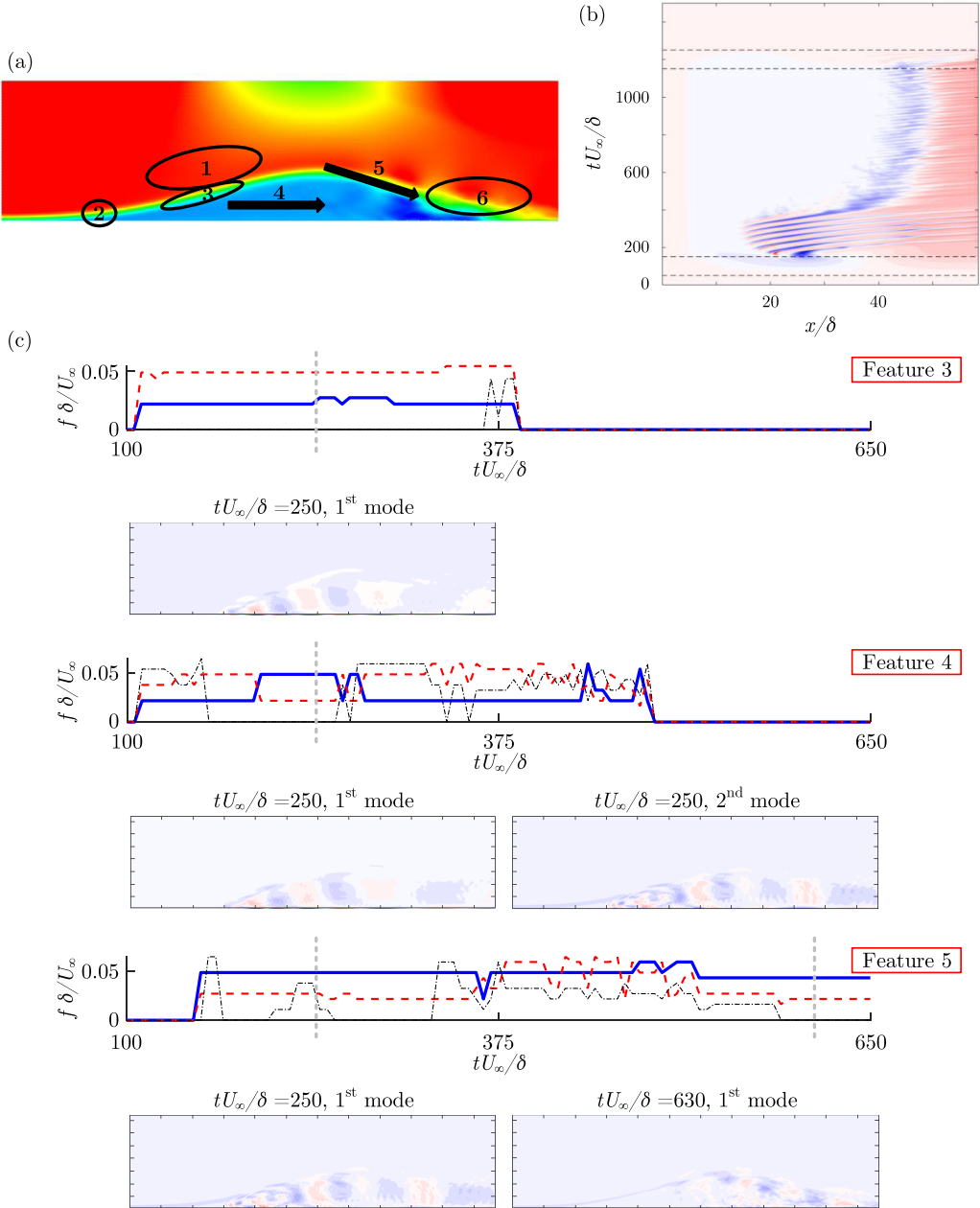
FIG. 16. (a) The location and trajectories of the six identified clusters, (b) the time-space plot of the surface friction coefficient, and (c) the leading frequencies of three representative clusters and the matching wDMD modes. The gray broken line denotes the moment the mode is plotted.

settles and a large separation bubble forms. In the meantime, the shear layer always remains intact and occurs after the separation bubble is established.

Here in Fig. 16, we also demonstrate how KMD can be served as a preconditioner for other modal analysis methods. To extract single-frequency contents, we will utilize a variant of the dynamic mode decomposition (DMD), Windowed DMD [3], which uses a temporally sliding window to

filter the data before performing DMD. Furthermore, the data is centered within each window following Hirsh *et al.* [30] to improve the identification of coherent structures from a transient response. One major issue of this method is the lack of mode significance differentiation, especially for less energetically prominent or locally confined modes. With the alignment energy map, we can track down the representative frequencies and match them to the wDMD modes with the same frequencies. Here we only show the modes that match the leading frequencies at a given time. We can see that the modes corresponding to cluster 3 explicitly represent the roll-up vortices that originate below the suction. The modes that share the same frequency with the dominant frequency of cluster 5 first look similar to the roll-up vortices, but they extend further downstream and are gradually absorbed into the shear layer associated with the established separation bubble. For cluster 4, an alternating appearance of both modes was detected. This further confirms our previous observation that two different mechanisms influence the roll-up phase, and once the s/b strength reaches a constant value, the shear effect takes over.

This section shows how the proposed KMD framework can be used to understand a complex engineering problem. With the spatial KMD framework, we discovered that the formation process of a laminar separation bubble at Re $\sim$ 865 is controlled by two modes stemming from different actuation mechanisms. It would be difficult for the classical modal analysis method to extract these competing modes when they are not only intertwined in space but also transition in amplitude and spatial distribution over time, and here KMD is proved to be a useful analysis tool for such a system.

VI. CONCLUSIONS AND REMARKS

KMD is a novel technique that can instigate the nonstationary response and provide better pattern recognition than classical methods. The method is extended to a spatial analysis by combining KMD with clustering in space and time utilizing the alignment energy, which indicates the similarity between the input signal and the fine modes. Three examples are used to demonstrate the effectiveness of the framework. The synthetic example consists of three Gaussian distributions pulsing at varying frequencies and amplitudes. For the canonical flow example, we showed a two-sided oscillating lid driven with different oscillation patterns for the two lids. Finally, the formation process of a laminar separation bubble with suction/blowing boundary conditions serves as an engineering example. In all three cases, the KMD framework successfully captures the spatial distribution and the varying frequencies of the transitioning modes. Specifically, in the separation bubble case, it identifies the mechanisms of two competing modes totally hidden from the classic modal analysis method.

The procedure presented in this paper is just one way to achieve KMD spatial analysis. We decided to utilize the alignment energy as the input for spatial and temporal clustering since it is a convenient by-product of the KMD process. Another possible route of doing spatial analysis is using high-dimensional wavelets to construct the fine mode bank to align with the entire domain. This approach is not followed in current research, but with sufficient computational resources, it could be a good alternative to DMD, which can only track stationary single-frequency modes. In the proposed KMD process, each step is physically amenable, which provides a specific advantage over the artificial neural network method, which often is a black box to the user. With sparsification, KMD allows local inquiry and global reconstruction in an interpretable way. Different clustering techniques can be adapted to fit different needs, and with the efficient 1D KMD, a wide range of frequencies and temporal localization can be considered for diverse applications. Moreover, the formation of a 1D KMD bank is fully parallelizable. Note that the computational cost is highly related to the resolution of the mode bank, which should discretize the interested range of the spatial distribution and frequencies. The actual computational cost in the operations falls mostly in calculating the alignment energy, which is an integral operation that scales with N in each parameter, which is also easily scalable with parallelization.

Another benefit of KMD is that it allows the use of nontrigonometric functions as the finer base mode, and in Owhadi *et al.* [15] both triangular and EKG waves, and a nonregular wave form, were used as examples. This procedure can be further expanded to add or substitute additional

characteristic values such as transition time, since the alignment energy calculation is not confined to frequency. For many common incompressible flow phenomena, oscillatory behavior is presented, and Gabor wavelets serve well as the base wave form with its localized nature, as demonstrated. For the follow-up research, we are working to demonstrate how different wave forms could represent other types of flow phenomena, such as shock.

In summary, the KMD technique allows the isolation of the transient modes based on the alignment energy, defined based on the similarity between the signal and the fine basis mode (Gabor wavelets are adopted in the current research). This is not an indicator of flow energy or dynamics but merely pattern recognition. Hence, the partition based on the alignment energy is not flow-energy based and has to be heuristically connected to the flow physics. A possible solution to this shortcoming could be using physically relevant flow features with different temporal and spatial characteristics as the fine mode banks, which can be readily implemented with the KMD setting. Nevertheless, as shown in the three examples, we believe that the KMD is powerful for dissecting complex dynamic fields. This procedure follows the spirit of the original KMD network as a robust and adaptive process.

[1] J. N. Kutz, X. Fu, and S. L. Brunton, Multiresolution dynamic mode decomposition, SIAM J. Appl. Dyn. Syst. **15**, 713 (2016).

[2] M. Mendez, M. Balabane, and J.-M. Buchlin, Multi-scale proper orthogonal decomposition of complex fluid flows, J. Fluid Mech. **870**, 988 (2019).

[3] H. Zhang, C. W. Rowley, E. A. Deem, and L. N. Cattafesta, Online dynamic mode decomposition for time-varying systems, SIAM J. Appl. Dyn. Syst. **18**, 1586 (2019).

[4] N. E. Huang, Z. Shen, S. R. Long, M. C. Wu, H. H. Shih, Q. Zheng, N.-C. Yen, C. C. Tung, and H. H. Liu, The empirical mode decomposition and the Hilbert spectrum for nonlinear and non-stationary time series analysis, Proc. R. Soc. London, Ser. A **454**, 903 (1998).

[5] P. J. Ansell and K. Mulleners, Multiscale vortex characteristics of dynamic stall from empirical mode decomposition, AIAA J. **58**, 600 (2020).

[6] D. A. Cummings, R. A. Irizarry, N. E. Huang, T. P. Endy, A. Nisalak, K. Ungchusak, and D. S. Burke, Travelling waves in the occurrence of dengue haemorrhagic fever in thailand, Nature (London) **427**, 344 (2004).

[7] C.-S. Lin, S.-H. Chiu, and T.-Y. Lin, Empirical mode decomposition–based least squares support vector regression for foreign exchange rate forecasting, Economic Modelling **29**, 2583 (2012).

[8] B. M. Battista, C. Knapp, T. McGee, and V. Goebel, Application of the empirical mode decomposition and Hilbert-Huang transform to seismic reflection data, Geophysics **72**, H29 (2007).

[9] D. Pines and L. Salvino, Structural health monitoring using empirical mode decomposition and the hilbert phase, J. Sound Vib. **294**, 97 (2006).

[10] A. Cochocki and R. Unbehauen, *Neural Networks for Optimization and Signal Processing* (John Wiley & Sons, Inc., New York, 1993).

[11] A. Stetco, F. Dinmohammadi, X. Zhao, V. Robu, D. Flynn, M. Barnes, J. Keane, and G. Nenadic, Machine learning methods for wind turbine condition monitoring: A review, Renewable Energy **133**, 620 (2019).

[12] T. Murata, K. Fukami, and K. Fukagata, Nonlinear mode decomposition with convolutional neural networks for fluid dynamics, J. Fluid Mech. **882**, A13 (2020).

[13] K. Fukami, R. Maulik, N. Ramachandra, K. Fukagata, and K. Taira, Global field reconstruction from sparse sensors with Voronoi tessellation-assisted deep learning, Nat. Mach. Intell. **3**, 945 (2021).

[14] M. Hutson, Has artificial intelligence become alchemy? Science **360**, 478 (2018).

[15] H. Owhadi, C. Scovel, and G. R. Yoo, *Kernel Mode Decomposition and the Programming of Kernels*, Surveys and Tutorials in the Applied Mathematical Sciences Vol. 8 (Springer, New York, 2021).

[16] T.-K. Wang and K. Shoele, Identification of transient modes during formation and detachment of a laminar separation bubble using kernel mode decomposition, in *AIAA Scitech 2021 Forum* (AIAA, Reston, VA, 2021), paper AIAA 2021-0248.

[17] C. Torrence and G. P. Compo, A practical guide to wavelet analysis, Bull. Am. Meteorol. Soc. **79**, 61 (1998).

[18] J. L. Lumley, The structure of inhomogeneous turbulent flows, in *Atmospheric Turbulence and Radio Wave Propagation*, edited by A. M. Yaglom and V. I. Tartarsky (1967), pp. 166–177.

[19] L. Sirovich, Turbulence and the dynamics of coherent structures, I. Coherent structures, Q. Appl. Math. **45**, 561 (1987).

[20] M. A. Mendez, D. Hess, B. B. Watz, and J.-M. Buchlin, Multiscale proper orthogonal decomposition (mPOD) of TR-PIV data—A case study on stationary and transient cylinder wake flows, Meas. Sci. Technol. **31**, 094014 (2020).

[21] T.-K. Wang and K. Shoele, Mode competition in a plunging foil with an active flap: A multiscale modal analysis approach, Phys. Rev. Fluids **7**, 044701 (2022).

[22] C.-H. Bruneau and M. Saad, The 2D lid-driven cavity problem revisited, Comput. Fluids **35**, 326 (2006).

[23] H. F. Oztop and I. Dagtekin, Mixed convection in two-sided lid-driven differentially heated square cavity, Int. J. Heat Mass Transf. **47**, 1761 (2004).

[24] S. R. Bhopalam, D. A. Perumal, and A. K. Yadav, Computational appraisal of fluid flow behavior in two-sided oscillating lid-driven cavities, Int. J. Mech. Sci. **196**, 106303 (2021).

[25] J. Molvar, 2D Lid Driven Cavity Flow Solver, MATLAB Central File Exchange. Retrieved June 6, 2023, https://www.mathworks.com/matlabcentral/fileexchange/77025-2d-lid-driven-cavity-flow-solver.

[26] J. H. Seo, F. Cadieux, R. Mittal, E. Deem, and L. Cattafesta, Effect of synthetic jet modulation schemes on the reduction of a laminar separation bubble, Phys. Rev. Fluids **3**, 033901 (2018).

[27] E. Aram, R. Mittal, and L. Cattafesta, Simple representations of zero-net mass-flux jets in grazing flow for flow-control simulations, Int. J. Flow Control **2**, 109 (2010).

[28] R. Mittal, H. Dong, M. Bozkurttas, F. Najjar, A. Vargas, and A. Von Loebbecke, A versatile sharp interface immersed boundary method for incompressible flows with complex boundaries, J. Comput. Phys. **227**, 4825 (2008).

[29] R. Richardson, T.-K. Wang, L. N. Cattafesta, and K. Shoele, Dynamics of a separation bubble subject to compliant surface motion, in *AIAA Aviation 2019 Forum* (AIAA, Reston, VA, 2019), paper AIAA 2019-3588.

[30] S. M. Hirsh, K. D. Harris, J. N. Kutz, and B. W. Brunton, Centering data improves the dynamic mode decomposition, SIAM J. Appl. Dyn. Syst. **19**, 1920 (2020).